Received: 3 August 2023 | Revised: 22 July 2024 | Accepted: 24 July 2024

DOI: 10.1002/qj.4835

RESEARCH ARTICLE

Quarterly Journal of the Royal Meteorological Society RMetS

Dealing with steep slopes when modeling stable boundary-layer flow in Alpine terrain

E. Le Bouëdec[1] | **C. Chemel**[2] | **C. Staquet**[1]

[1]Université Grenoble Alpes, CNRS, Grenoble INP, LEGI, Grenoble, France

[2]National Centre for Atmospheric Science, University of Leeds, Leeds, UK

Correspondence
C. Chemel, National Centre for Atmospheric Science, University of Leeds, Fairbairn House, 71–75 Clarendon Road, Leeds LS2 9PH, UK.
Email: charles.chemel@ncas.ac.uk

Funding information
French National Research Agency, Grant/Award Number: ANR-15-IDEX-02

Abstract

Steep slopes in mountainous terrain are challenging for commonly used numerical weather prediction models using terrain-following coordinates since they can generate numerical errors when evaluating horizontal gradients, and numerical instabilities. The model orography is therefore generally smoothed locally so as to remove slopes exceeding a defined threshold, typically in the range 30°–40°. However, this process can lead to undesired changes to orographic features at the scale of the mountain range. So as to preserve properties of the orography, e.g., mean terrain height across the domain, a global smoothing algorithm is developed. The algorithm is then applied to a domain centred on the Alpine Grenoble valley. Exploration of the parameters of the algorithm allows to minimize the changes in the orography in the domain, especially that of the two main valleys (of width 2 and 5 km and depth about 2000 m). Results of numerical model simulations are next analyzed to evaluate the effects of the slope threshold on local- and valley-scale atmospheric dynamics for a cold-air pool episode. Model results from simulations with slope thresholds of 28° and 42° are compared, the lower threshold allowing for a reduction (albeit small in practice) of the near-surface vertical grid spacing. Remarkably, not only are the near-surface boundary-layer temperature and wind fields similar for both simulations (and in very good agreement with observations), but this similarity holds in the whole inversion layer throughout the episode. The reasons for this similarity are that, for this cold-air pool episode, the valley atmospheric dynamics is confined within the inversion layer and the orography is essentially unchanged by the smoothing algorithm in that layer for the slope threshold of 28° and 42°.

KEYWORDS

cold-air-pool episode, mountainous terrain, smoothing of orography, WRF model

1 | INTRODUCTION

Atmospheric boundary-layer flows are the result of exchanges of mass and energy between the near-surface air and the ground. Over land the dynamics of these flows are sensitive to spatial variations in the elevation of the terrain and in its cover and soil properties. Such topographic variations translate into inhomogeneity of the mean flow and of turbulence, which are determinant for a range of applications, including air pollution, aviation meteorology, and wind energy harvesting.

The effects of these variations on the mountain boundary-layer dynamics depend on the large-scale flow. Large-scale flows approaching a mountain range respond to features of the orography at the scale of the range rather than at the smaller scale of orographic details. The upstream large-scale flow can be blocked or channeled by orographic features. When large-scale winds are weak across the orography, leading to a dynamical decoupling between the boundary layer in valleys and the free atmosphere, the structure and evolution of the boundary layer are determined to a large extent by the thermally driven flows induced by topographic variations of all scales. On clear-sky nights, cooled near-surface air sinks to valley bottoms, thereby creating strongly stably stratified valley boundary layers. These cold-air pools can persist for multiple days, especially in winter when surface heating is insufficient during daytime to destabilize the stable boundary layer and when warm air is advected above it (Arduini *et al.*, 2020; Lu & Zhong, 2014; Reeves & Stensrud, 2009; Vrhovec & Hrabar, 1996). In urbanized valleys, such cold-air pools can lead to an accumulation of air pollution, which can lead to severe air pollution episodes (Chemel *et al.*, 2016; Largeron & Staquet, 2016; Quimbayo-Duarte *et al.*, 2021; Silcox *et al.*, 2012; Whiteman *et al.*, 2014). Simulating accurately such conditions in narrow and deep terrain using numerical weather prediction (NWP) models is very challenging, particularly because of steep slopes (see for instance Zhong & Chow, 2013).

Let us consider that the effective spatial resolution of an NWP model is $p\,\Delta x$, where Δx is the horizontal grid spacing. By comparing kinetic energy spectra with observations in the inertial range, Skamarock (2004) estimated the value of the parameter p to be 7 for the Weather Research and Forecasting (WRF) model, used in the present work. Resolving the flow at the scale of a valley then requires $\Delta x \ll L/p$, where the length scale L of the valley can be taken as the width of the valley floor. Hence, for the WRF model with $p = 7$, a relatively narrow valley such as the Grésivaudan valley, with $L \approx 3500$ m, demands horizontal grid spacings $\Delta x \ll 500$ m (e.g., $\Delta x \sim 100$ m). The Grésivaudan valley is the northeast branch of the Grenoble valley in the French Alps, considered therein; see Figure 1.

For a given vertical grid spacing, the finer the horizontal grid spacing the steeper the resolved slopes can be. Moreover, steep slopes result in highly skewed grids near the surface for models using terrain-following coordinates, which include most commonly used NWP models (such as the WRF model). Such distorted grids can generate significant numerical errors when evaluating horizontal gradients (Connolly *et al.*, 2021; Klemp *et al.*, 2003; Mahrer, 1984; Zängl *et al.*, 2004), and numerical instabilities. The slope stability limit that follows from using terrain-following coordinates can be expressed as (Connolly *et al.*, 2021)

$$\tan(\phi_{\max}) < b\frac{\Delta z}{\Delta x}, \tag{1}$$

for a maximum slope angle $\phi_{\max}$ with a vertical grid spacing Δz, where b is an empirically estimated parameter with acceptable value in the range 1–5 (Connolly *et al.*, 2021; Zhong & Chow, 2013). For a given Δx, steep slopes therefore severely limit the refinement of vertical grid spacings near the surface, such that

$$\Delta z > \tan(\phi_{\max})\frac{\Delta x}{b}. \tag{2}$$

Taking $\Delta x = 100$ m, $\phi_{\max} \approx 60°$ on a section of the southeast-facing sidewall of the Grésivaudan valley, and $b = 3$ (Connolly *et al.*, 2021), one gets $\Delta z \gtrapprox 58$ m, which is undoubtedly too coarse to resolve near-surface thermally driven flows.

Numerical model simulations of the atmospheric boundary layer of real Alpine valleys with horizontal grid spacings Δx of order 100 m are very few and recent. To allow for a finer vertical resolution near the surface while keeping the model numerically stable for these simulations, the model orography is generally smoothed locally so as to remove steep slopes exceeding a defined threshold—for example, 45° in Arduini *et al.*, 2020 or 42° in Quimbayo-Duarte *et al.*, 2021 and Umek *et al.*, 2021; see also Sheridan *et al.*, 2023. Such local smoothing of the orography can alter the overall shape of the terrain of the region of interest and, as a result, can possibly lead to a response of the atmospheric flow that is different to that of the real (unsmoothed) terrain.

In this article we develop a global smoothing algorithm designed to preserve properties of the orography (e.g., mean terrain height across the domain). This algorithm is presented and applied to the orography of the Grenoble valley in Section 2. The remainder of the article aims at evaluating the impact of the smoothed orography on the flow dynamics for a cold-air pool episode in this valley. To this aim, two different values for the maximum slope angle of the orography, 28° and 42°, are considered. The set-up of the WRF model is presented in Section 3, and the flow structure and properties both locally and at the scale of the valley are analyzed and compared in Section 4. Conclusions are given in Section 5.

2 | SMOOTHING OF THE MODEL OROGRAPHY

2.1 | Description of the optimization problem

Let us define $\mathbf{h}_0$ as the original terrain height once interpolated on the model grid of size (nx, ny). Let us

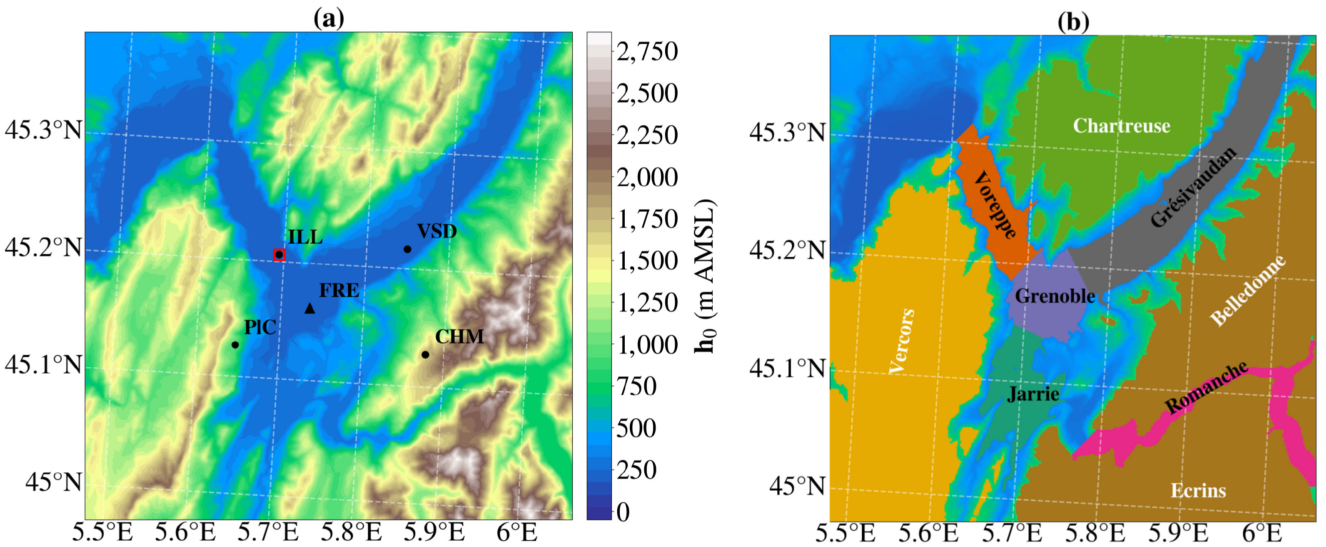

FIGURE 1 (a) Terrain height $\mathbf{h}_0$ (above mean sea level, AMSL) for the innermost domain grid considered in Section 3, with horizontal grid spacing $\Delta x = \Delta y = 111$ m, derived by interpolation of the 30-m terrain elevation data from the Shuttle Radar Topography Mission (SRTM, Farr *et al.*, 2007). The measurement sites used for the model evaluation and presented in Section 4.1 are indicated by symbols: red square for wind (Institut Laue-Langevin, ILL), black circles for temperature (Chamrousse, CHM; ILL; Peuil de Claix, PlC; Le Versoud airfield, VSD), and black triangle for air pollution (Les Frenes, FRE) measurement stations. The main characteristics of these stations are indicated in Table 2. (b) Naming convention used for the main valleys (black lettering) and massifs (white lettering) within the domain.

also denote by $\overline{\mathbf{h}}$ the target smoothed terrain height respecting some constraints. The constraints are defined here as a maximum angle $\phi_{\max}$ allowed for the slopes of the target orography along the x and y horizontal directions and along their diagonal directions.

By considering the terrain height for each grid point as a variable, then the problem has $nx \times ny$ degrees of freedom. Let us denote by $\vec{a}$ the vector of length $nx \times ny$ populated with all the values in $\mathbf{h}_0$ and introduce the operator, denoted vec, such that $\vec{a} = \mathrm{vec}(\mathbf{h}_0)$. Let us also introduce the factor $\vec{q}$, a vector of size $nx \times ny$, by which $\vec{a}$ must be multiplied in order to obtain the smoothed orography ($\overline{\mathbf{h}}$), such that

$$\vec{a} \odot \vec{q} = \mathrm{vec}(\overline{\mathbf{h}}), \tag{3}$$

where $\vec{a} \odot \vec{q}$ is the vector of components $a_i q_i$, and the vector $\vec{q}$ is determined by the optimization problem

$$\begin{cases} \text{Minimize} & \mathcal{F} = \|\vec{a} \odot \min(\vec{q} - \vec{1}, 0) \times n\|^2 \\ & +\|\vec{a} \odot \max(\vec{q} - \vec{1}, 0) \times m\|^2, \\ \text{such that} & \max(|\nabla_x \overline{\mathbf{h}}|/\Delta x) \leq \tan \phi_{\max}, \\ \quad \text{and} & \max(|\nabla_y \overline{\mathbf{h}}|/\Delta y) \leq \tan \phi_{\max}, \\ \quad \text{and} & \max(|\nabla_{d_1} \overline{\mathbf{h}}|/\sqrt{\Delta x^2 + \Delta y^2}) \leq \tan \phi_{\max}, \\ \quad \text{and} & \max(|\nabla_{d_2} \overline{\mathbf{h}}|/\sqrt{\Delta x^2 + \Delta y^2}) \leq \tan \phi_{\max}, \end{cases} \tag{4}$$

where $\vec{1}$ is the identity vector (with all components equal to 1), $\{n, m\} \in \mathbb{N}^\star$ are penalization factors, Δx and Δy are the grid spacings in the x and y directions respectively, ∇_x and ∇_y are the gradient operators along the x- and y-axis respectively, and ∇_{d_1} and ∇_{d_2} are the gradient operators along the two horizontal diagonal axes. If no constraint is saturated in the original orography, then $\vec{q}$ is the identity vector, giving a null cost function ($\mathcal{F} = 0$) and resulting in no modification of the orography.

The penalization factors n and m in the cost function allow for a finer control over the resulting orography. If $m > n$, grid points that are higher in the smoothed orography than in the original orography ($q_i > 1$) are penalized more than those that are lower ($q_i < 1$). This results in a smoothed orography where the altitude of valley floors is better preserved at the cost of lowering more the surrounding terrain. Conversely, if $m < n$, the peaks are better preserved, but this requires an increase in height for certain parts of the terrain (such as valley floors). It is worth noting that the cost function as defined here is based only on the difference in terrain height with respect to the original terrain. Other mathematical formulations can be envisaged to preserve other properties of the terrain, such as the curvature.

2.2 | Application to the orography of the Grenoble valley

The Grenoble valley, located between the Alpine massifs of Vercors, Chartreuse, and Belledonne (see Figure 1), is characterized by steep sidewalls (see Figure 2), with

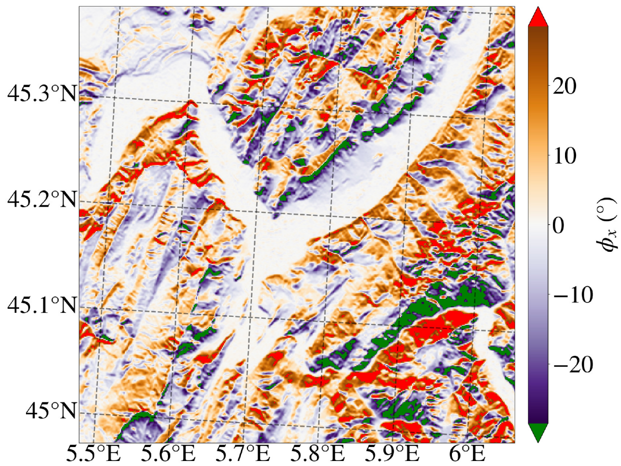

FIGURE 2 Angle of the slope of the orography in the x direction, $\phi_x = \arctan(\nabla_x \mathbf{h}_0)$, for the same domain and dataset as those of Figure 1a.

slopes exceeding 60°. The optimization problem defined in Section 2.1 is solved for the grid of the domain shown in Figure 1 for a few values of n and m and $\phi_{\max}$ in the range 10°–50°. The domain contains 202×202 grid points with horizontal grid spacing $\Delta x = \Delta y = 111$ m.

Figure 3 displays the fraction of the grid with slopes higher than a given value of $\phi_{\max}$ (i.e., the fraction smoothed by the algorithm) and the change in the mean terrain height over the domain as a function of $\phi_{\max}$ for $n = m = 1$. As expected, the smaller the slope threshold $\phi_{\max}$ is, the greater is the fraction of the domain grid that needs smoothing of the original orography (orange solid line), the greater is the change in mean terrain height across the domain between the original and smoothed orographies (blue dashed line with dots). We select the maximum slope thresholds $\phi_{\max} = 28°$ and 42° for the subsequent analysis, for which 20% and 3% of the domain grid respectively have slopes greater than $\phi_{\max}$. For $\phi_{\max} = 28°$ and 42°, the differences in mean terrain height across the domain between the original and smoothed orographies are 15.3 m and 1.6 m respectively. This difference increases rapidly for $\phi_{\max} < 28°$ as $\phi_{\max}$ decreases.

To further show the potential of the smoothing algorithm, the case for $\phi_{\max} = 28°$ is also considered in Figure 4 for $n < m$ and in Figure 5 for $n < m$ and $n > m$; for $n < m$ ($m < n$), it is more cost-effective to lower (raise) the orography than to raise (lower) it. These smoothed orographies are compared in the following in terms of differences in terrain height and slope distribution. Hereafter, smoothed orographies follow the naming convention `tXXnImJ`, whereby `XX`, `I`, and `J` are the values of $\phi_{\max}$, n, and m respectively.

Figure 4 shows the differences in terrain height between the original and smoothed orographies for the configurations `t28n1m1`, `t28n1m5`, and `t42n1m1`. For those configurations, only the massifs surrounding the Grenoble valley are affected by the smoothing; the Grenoble valley floor remains untouched. As expected, the orography for `t42n1m1` is much less affected than that for `t28n1m1` (as is quantified in Figure 5). Indeed, the massifs of Vercors and Chartreuse remain unchanged except locally for the vertical cliffs that border them. Note that the cliffs are smoothed over more grid points for `t28n1m1` than for `t42n1m1`.

Figure 4 also shows that the very narrow and deep Romanche tributary valley (see Figure 1b for the location of the Romanche valley), with bottom width of about 1 km and depth of about 2000 m, is nevertheless subject to a significant smoothing, especially for `t28n1m1`. For the original orography of the domain shown in Figure 1, the altitude of the valley floor varies from 300 m to 800 m, and the altitude of the surrounding peaks is about 2400 m. For `t42n1m1` the valley floor is raised by up to 287 m and the peaks are lowered by up to 185 m. For `t28n1m1` the Romanche valley floor is raised by up to 393 m and the surrounding peaks are lowered by as much as 515 m. The introduction of a penalization with $m > n$ allows the algorithm to be steered so as to preserve better the height of the valley floor. This is important for the representation of the simulated temperature differences between the Romanche valley and the Grenoble valley. Thus, for `t28n1m5` the Romanche valley floor is raised by at most 138 m, but the surrounding peaks are then lowered by up to 731 m. Smoothing the orography in this part of the Grenoble valley is thus a challenging task.

The percentile distribution of the difference in terrain height between the original orography and the smoothed orographies is shown in Figure 5 for `t28n1m1`, `t28n2m1`, `t28n1m2`, `t28n1m5`, and `t42n1m1`. The best configuration is obtained for $\phi_{\max} = 42°$ and $n = m = 1$, with at most 5% of the grid points departing from their original heights after smoothing. By contrast, this ratio reaches 20% for the configuration `t28n1m1`, with about half of the grid points being lowered and the other half raised, consistent with the absence of penalization in the algorithm ($n = m = 1$). Penalization leads to the largest terrain height differences, with a positive bias for $m > n$ and a negative bias for $n > m$.

Figure 6 compares the distribution of slopes in the x and y directions for the original orography and the smoothed orographies for `t28n1m1` and `t42n1m1`. The smoothing algorithm cuts effectively the tails of the distributions at the threshold values, thereby generating peaks in the distributions. These peaks are more clearly marked for $\phi_{\max} = 28°$ than for $\phi_{\max} = 42°$ since a larger fraction of the grid is concerned by the smoothing. Additional peaks may be noticed (especially for $\phi_{\max} = 28°$). These additional peaks are generated when constraints on both the diagonal and either the x or y

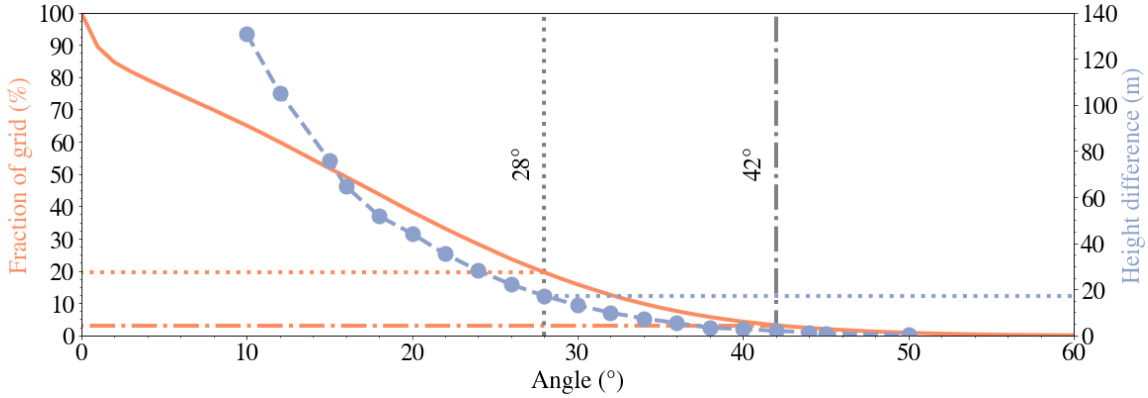

FIGURE 3 Analysis of the solution of the optimization problem defined in Section 2.1 with $n = m = 1$ for the orography of the domain shown in Figure 1. The x-axis indicates the threshold angle, referred to as $\phi_{\max}$ in Section 2.1. The orange curve represents the fraction of the grid of the domain with slopes greater than $\phi_{\max}$ (which has been smoothed). The blue curve represents the differences in mean terrain height over the domain between the original and the smoothed orography for the threshold angle $\phi_{\max}$. The left and right axes relate to the orange and blue curves respectively. The horizontal and vertical dotted and dash-dotted lines are visual guides to extract quantitative figures for the values of the fraction of the grid that has been smoothed and mean terrain height difference for $\phi_{\max} = 28°$ and 42°.

axis are saturated. Indeed, if two of the sides of a triangle are constrained, the third side is geometrically imposed. These peaks match exactly the slope angle corresponding to the non-saturated constraint, viz.

$$\phi_s = \arctan\left[\tan(\phi_{\max}) \times \left(\frac{2}{\sqrt{2}} - 1\right)\right]. \quad (5)$$

These secondary peaks emphasize the effect of taking into account diagonal constraints when smoothing the orography. Otherwise, constraints along both the x and y axes could be saturated simultaneously, which could lead to unwanted steep diagonal slopes (for instance, diagonal slopes as large as 46.7° for $\phi_{\max} = 28°$).

3 | DESIGN OF THE NUMERICAL EXPERIMENTS

As stressed in Section 1, the remainder of the article aims at evaluating the impact of the smoothed orography on the flow dynamics for a cold-air pool episode in the Grenoble valley. The motivation for selecting the slope threshold $\phi_{\max}$ is first discussed. The choice of the simulated episode is next presented briefly followed by the description of the WRF model set-up required to simulate this episode.

3.1 | Compromise between vertical resolution and steepness of the terrain

Figures 4 and 5 show that for fixed values of n and m the larger is the slope threshold $\phi_{\max}$ the more accurate is the description of the orography. However, the slope stability limit imposes coarser vertical grid spacings. So as to resolve the flow within the Grenoble valley in a reliable manner, the finest possible vertical resolution is desirable. Hence, a compromise between vertical resolution and steepness of the terrain is required. The minimum value of Δz for a given $\phi_{\max}$ is estimated from Equation (1). Taking $\Delta x = 111$ m and as in Connolly *et al.* (2021) $b = 3$, Equation (1) yields $\Delta z > 33$ m for $\phi_{\max} = 42°$ and $\Delta z > 20$ m for $\phi_{\max} = 28°$. These predictions nearly match what is found in practice by trial and error: one needs $\Delta z > 32$ m for $\phi_{\max} = 42°$ and $\Delta z > 25$ m for $\phi_{\max} = 28°$ to keep the WRF model numerically stable (see Section 3.3). Hence, reducing $\phi_{\max}$ from 42° to 28° allows a reduction (albeit modest) of the vertical grid spacings. In Section 4, model results from simulations with slope thresholds of 28° and 42° are compared.

3.2 | Choice of the simulated cold-air pool episode

Le Bouëdec (2021) has shown that wintertime particulate air pollution episodes in the Grenoble valley are generally associated with the development of persistent cold-air pools under the Scandinavian blocking wintertime weather regime over the Euro-Atlantic region (e.g., Hannachi *et al.*, 2017). We select one such episode that occurred from December 1 to 6, 2016. The top panel in Figure 7 shows that during this episode the region of high pressure (anomaly) was not entirely stationary but moving slowly eastward from the British Isles to eastern Europe. The bottom panel of the figure indicates that the large-scale winds were weak above the Grenoble valley, at most 10 m·s^{-1} during the period December 2–6, 2016, a situation conducive to a cold-air-pool episode.

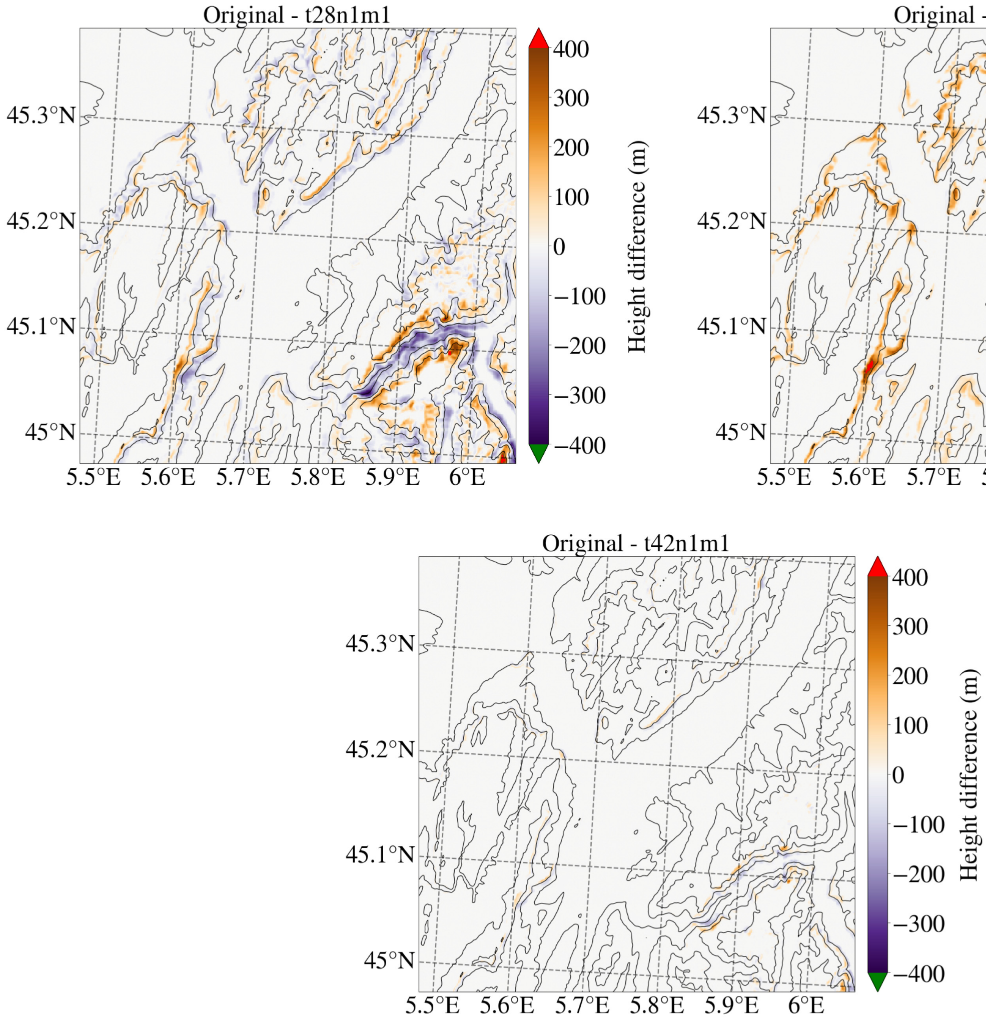

FIGURE 4 Differences in terrain height for the domain shown in Figure 1, between the original orography and the orography smoothed by solving the optimization problem defined in Section 2.1, for the configurations `t28n1m1`, `t28n1m5`, and `t42n1m1` (see Section 2.2 for details of these configurations). The thin black lines represent isolines of the terrain height, every 500 m, for the original orography.

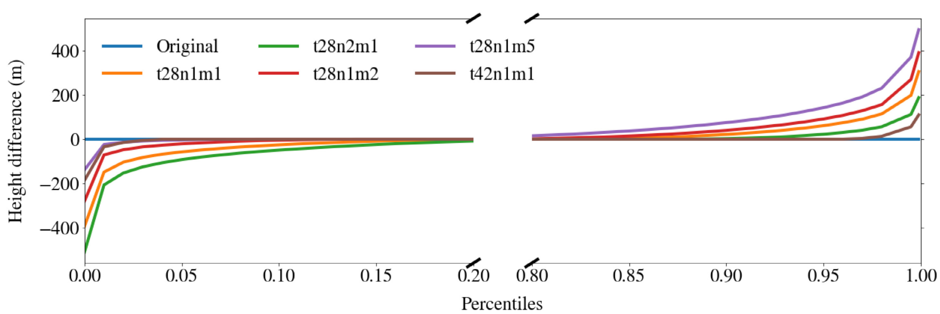

FIGURE 5 Percentile distribution, for the domain shown in Figure 1, of the differences in terrain height between the original orography and that smoothed by solving the optimization problem defined in Section 2.1 for the configurations `t28n1m1`, `t28n2m1`, `t28n1m2`, `t28n1m5`, and `t42n1m1` (see Section 2.2 for details of these configurations).

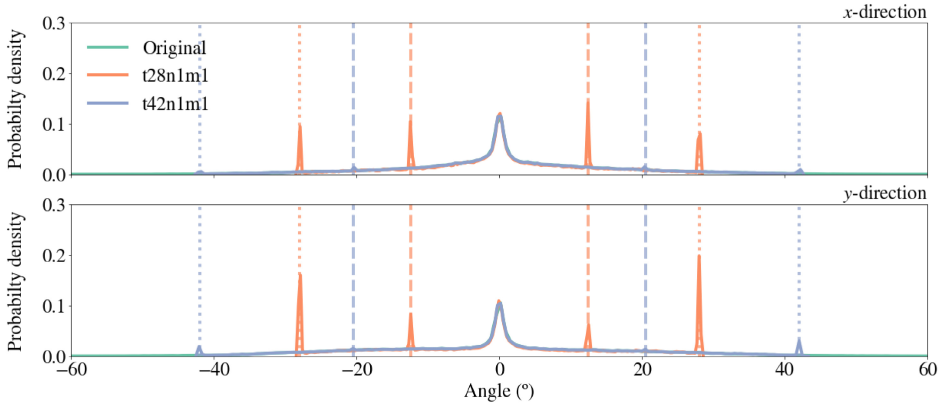

FIGURE 6 Distribution of slopes in the x and y directions for the domain shown in Figure 1, for the original orography and the orographies smoothed by solving the optimization problem defined in Section 2.1 for the configurations `t28n1m1` and `t42n1m1` (see Section 2.2 for details of these configurations). The dotted and dashed vertical lines indicate the slope threshold ϕ_{max} and the angle ϕ_s computed from Equation (5) respectively, for each configuration.

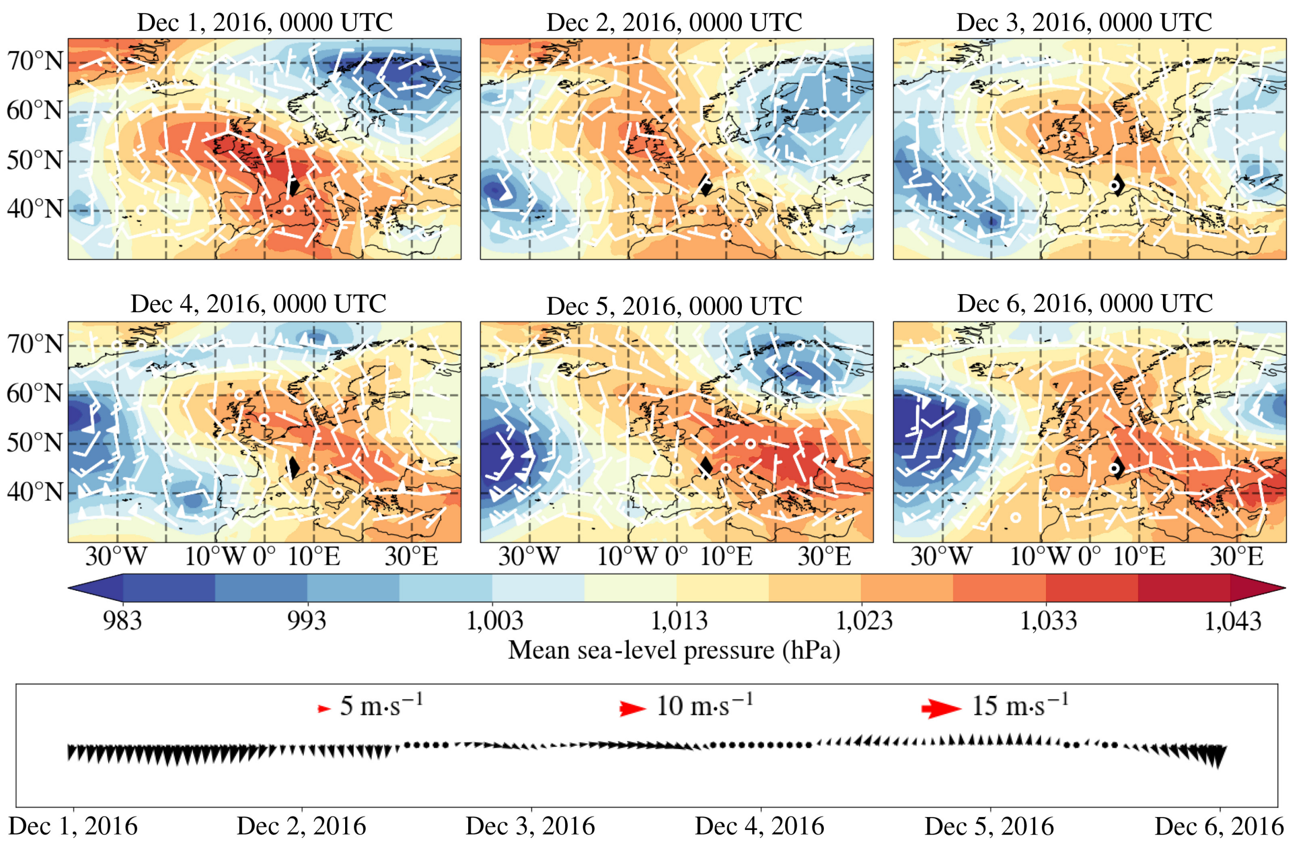

FIGURE 7 Synoptic weather conditions on December 1–6, 2016, at 0000 UTC, extracted from the gridded European Centre for Medium-range Weather Forecasts Reanalysis v5 with a horizontal resolution of about 30 km. Top panel: sea-level pressure (color contours) and wind barbs at 700 hPa. The black diamond in the weather charts indicates the position of the Grenoble valley (45.25°N, 5.75°E). Bottom panel: time series of wind speed and direction at 700 hPa at this location.

The episode was characterized by hourly PM_{10} (suspended particulate matter with aerodynamic diameters less than 10 μm) concentrations at the urban background site of "Les Fresnes" (FRE) in the Grenoble valley (see Figure 1 for the location of the site) in the range 28–66 $\mu g \cdot m^{-3}$. The episode-averaged PM_{10} concentration at this site was 43 $\mu g \cdot m^{-3}$ (nearing the daily average limit value of 50 $\mu g \cdot m^{-3}$ required by the European Directive 2008/50/EC on ambient air quality and cleaner air for Europe not to be exceeded for more than 35 days in a calendar year).

3.3 | Description of the domains and the initialization

As justified in Section 1, a horizontal resolution $\Delta x \sim$ 100 m is required to resolve the flow at the scale of the Grenoble valley. To achieve this resolution, four nested

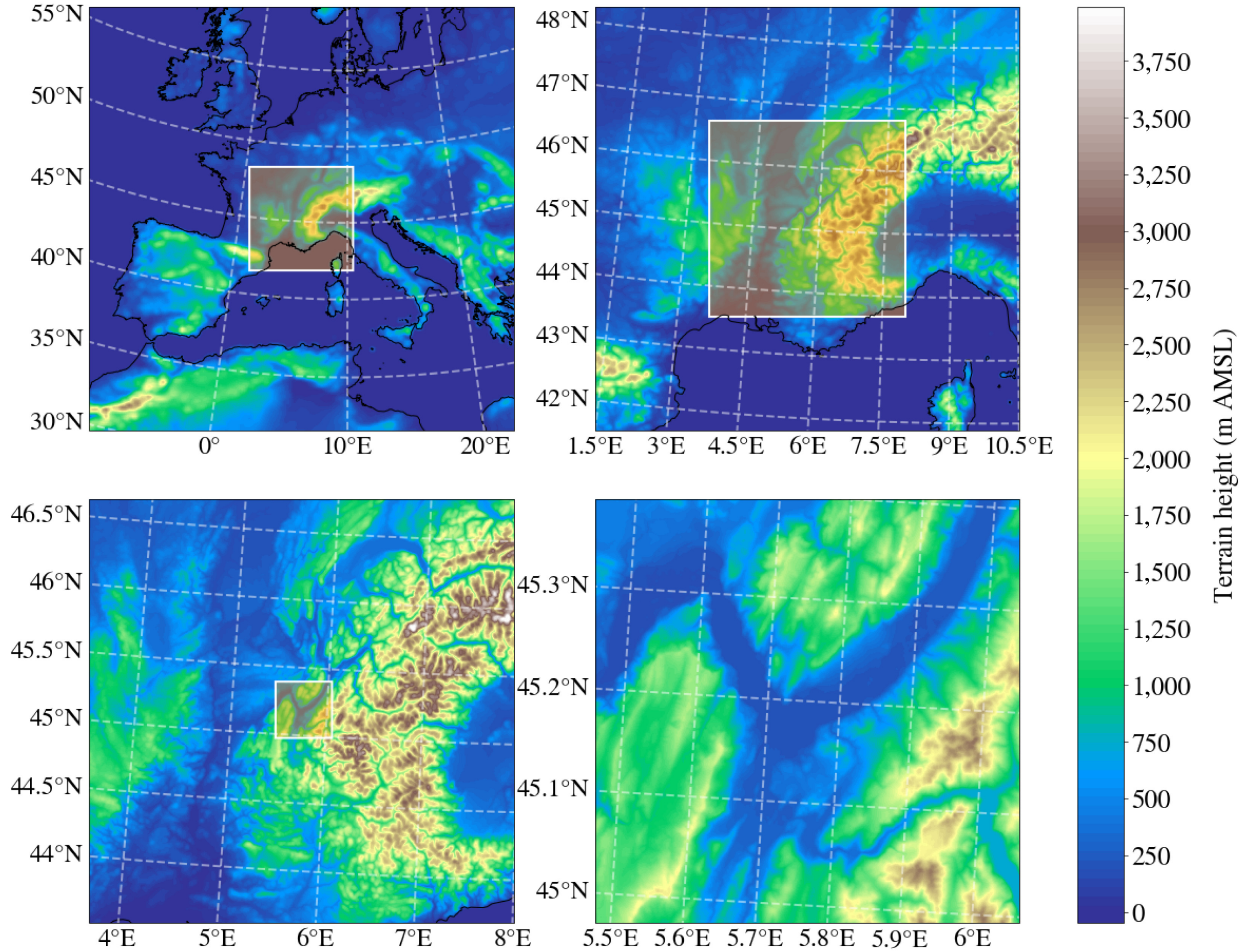

FIGURE 8 Geographical extent and orography of the four nested domains used for the simulations performed in the present work. The inner white-edged squares indicate the areas covered by the subsequent nested domains.

domains with respective Δx of 15, 3, 1, and 0.111 km are used. Their geographical extent and orography are depicted in Figure 8, and Table 1 provides additional information for each domain. The orography for each domain grid is obtained by interpolation of the 30-m terrain elevation data from the Shuttle Radar Topography Mission (SRTM, Farr *et al.*, 2007). Only the innermost domain orography contains very steep slopes (exceeding 28°) and hence is smoothed by solving the optimization problem defined in Section 2.1. Simulations were performed for the configurations `t28n1m1` and `t42n1m1` (see Section 2.2) and are compared in Section 4; the configuration `t28n1m5` is also considered in Section 4.3. As discussed in Section 3.1 (see also Table 1), these simulations have the same horizontal grid spacing but small differences in vertical resolution.

The land cover was prescribed using the CORINE Land Cover dataset from 2018, which covers the majority of Europe at 100 m horizontal resolution (Büttner, 2014). This dataset is commonly used in NWP models for domains covering Europe (e.g., Santos-Alamillos *et al.*, 2015; Umek *et al.*, 2021). As it uses its own land-cover categories, it has been remapped, for convenience, to the United States Geological Survey land-cover categories used in the WRF model, following the approach proposed

TABLE 1 Information for each nested domain used for the simulations performed in the present work: horizontal resolution Δx, near-surface vertical grid spacing Δz_s, equal to 25 m for the configuration `t28n1m1` and to 32 m for the configuration `t42n1m1` (see Section 2.2 for details of these configurations), number of grid points in the x, y, and z directions nx, ny, nz, and time step Δt.

Domain	Δx (km)	Δz_s (m)	nx, ny, nz	Δt (s)
d01	15	25 or 32	202, 202, 91	60
d02	3	25 or 32	246, 246, 91	12
d03	1	25 or 32	340, 340, 91	4
d04	0.111	25 or 32	406, 406, 91	0.2

by Pineda *et al.* (2004). The resulting land cover is shown for the innermost domain d04 in Figure 9a.

The computations were made on 91 vertical layers stretched in the vertical with a model top at 50 hPa. The vertical grid spacing near the ground surface $\Delta z_s \approx 25$ m above ground level (AGL) for `t28n1m1` and ≈ 32 m AGL for `t42n1m1` (such that the first mass point above the surface is approximately at 12.5 m for `t28n1m1` and 16 m for `t42n1m1`). This near-surface vertical resolution was required to keep the WRF model numerically stable (see Section 3.1).

The simulations were run continuously for the time period from December 1 to December 6, 2016. Initial conditions other than those for the snow fields (see later), and lateral boundary conditions for the outermost domain d01, were derived from the gridded European Centre for Medium-range Weather Forecasts Reanalysis v5 (ERA5) available every hour with a horizontal resolution $\Delta x \approx 30$ km. Lateral boundary conditions for d02–d03 were updated every parent-domain time step (using one-way nesting). To minimize the deviation of the WRF model solution from ERA5, spectral nudging was used for domain d01.

By default the snowpack would be initialized from the ERA5 dataset. However, the relatively coarse horizontal resolution of this dataset ($\Delta x \approx 30$ km) is not suitable for downscaling to much smaller scales. Errors in the snowpack initialization can lead to non-negligible discrepancies between simulations and measurements. For instance, Tomasi *et al.* (2017) showed that using the WRF model with a coarsely initialized snow albedo can lead to substantial underestimation of near-surface (2 m) temperature.

Following Arduini (2017), the MODIS/Terra (MOD10 L2) satellite product for snow extent and albedo available at a horizontal resolution of 500 m was used to initialize the snowpack prognostic variables. Since cloud cover can prevent satellite observations, observations from the previous five days were also considered so that missing data could be completed. Snow cover is non-zero when snow albedo is non-zero. Snow age was then determined by inverting an empirical function fitted in Livneh *et al.* (2010). Snow height was computed using an empirical function based on altitude, and the resulting field is shown in Figure 9b. Snow density cannot be retrieved directly as a function of snow albedo, as shown by Bohren and Beschta (1979), and hence was roughly estimated from snow age through another empirical function derived from Meløysund *et al.* (2007).

3.4 | Dynamical core

The Advanced Research WRF (version 4.1) dynamical core (Skamarock *et al.*, 2019) is used in this work. The WRF model is mainly designed for simulations at mesoscale where the horizontal resolution is typically ranging from $\mathcal{O}(100$ m$)$ to $\mathcal{O}(100$ km$)$. The Advanced Research WRF dynamical core solves an Eulerian, fully compressible and non-hydrostatic version of the Navier–Stokes equation using a terrain-following coordinate system. A third-order Runge–Kutta scheme is used for time integration. The time step Δt associated with time integration for each nested

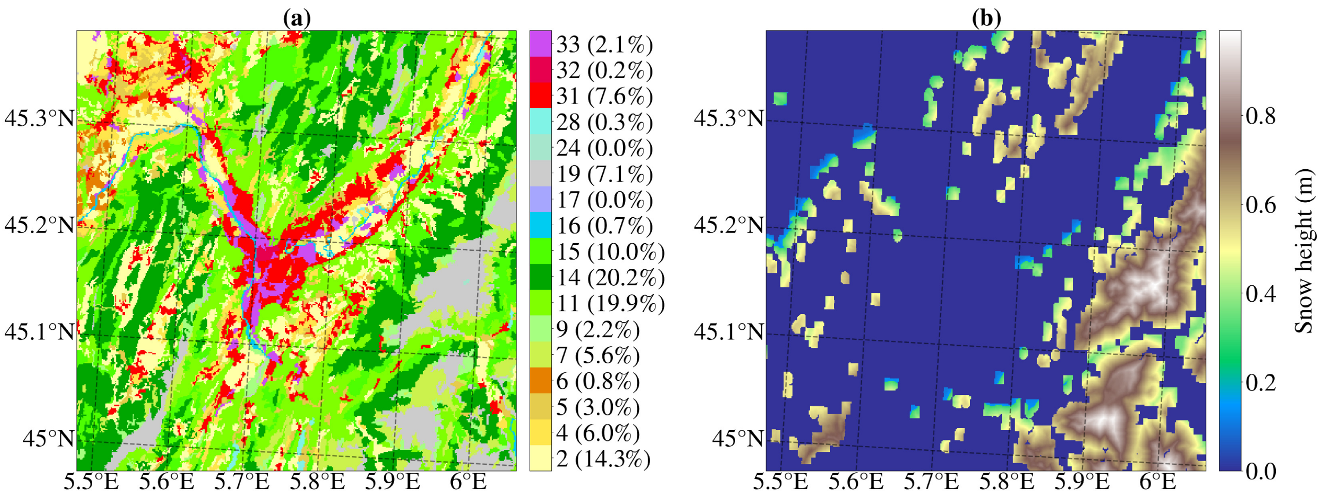

FIGURE 9 (a) Spatial distribution of the land-cover types for the innermost domain. The land-cover types are as follows: (2) Dryland cropland and pasture; (4) Mixed dryland/irrigated cropland and pasture; (5) Cropland/grassland mosaic; (6) Cropland/woodland mosaic; (7) Grassland; (9) Mixed shrubland/grassland; (11) Deciduous broadleaf forest; (14) Evergreen needleleaf forest; (15) Mixed forest; (16) Water bodies; (17) Herbaceous wetland; (19) Barren or sparsely vegetated; (24) Snow or ice; (28) Lakes; (31) Low-intensity residential; (32) High-intensity residential; and (33) Industrial or commercial. The fraction of each land-cover type across the domain is indicated in parentheses in the color bar. (b) Spatial distribution of snow height used as initial condition on December 1, 2016, for this domain.

domain is given in Table 1. The model uses a time-splitting technique to integrate the acoustic modes with an acoustic time step δt, which we set to $\Delta t/10$. A fifth-order weighted essentially non-oscillatory advection scheme is used for both vertical and horizontal advection, which is defined as monotonic for positive-definite variables.

3.5 | Physics parametrizations

The horizontal resolution $\Delta x \geq 1$ km for domains d01–d03 is much coarser than the vertical resolution, such that mixing in the planetary boundary layer by subgrid-scale (SGS) turbulence is primarily driven by vertical motions, and hence is assumed to be decoupled from horizontal mixing. Several studies compared the performance of planetary boundary layer mixing parametrization schemes (Marjanovic *et al.*, 2014). For example, Xie *et al.* (2012) and Deppe *et al.* (2013) showed that the differences between the schemes are generally modest, but the Yonsei University scheme (Hong *et al.*, 2006) ranks among the best-performing schemes. Based on this result, this scheme is chosen. Horizontal SGS turbulence is parametrized using the first-order Smagorinsky turbulence closure scheme (Smagorinsky, 1963). For domain d04 with $\Delta x = 0.111$ km (see Table 1), the 1.5-order turbulence closure scheme developed by Deardorff (1980) is used, which involves a prognostic equation for the three-dimensional SGS turbulent kinetic energy.

The simulations use the double moment microphysics parametrization scheme developed by Morrison *et al.* (2009), with the number of cloud condensation nuclei increased to 500 cm^{-3}, a value representative of continental environments, the Rapid Radiative Transfer Model for Global climate models short- and long-wave radiation parametrization schemes (Iacono *et al.*, 2008) and the community Noah land surface model (Chen & Dudhia, 2001).

The Monin–Obukhov similarity theory (Jiménez *et al.*, 2012) is used to couple the land surface to the atmosphere. Moreover, the slope effect on radiation and the topographic shading are also considered. Urban areas are treated as impervious surfaces with increased roughness using the bulk parametrization scheme described by Liu *et al.* (2006).

4 | RESULTS AND ANALYSIS

The objective of this section is to compare the impact of the orography, smoothed using a maximum slope angle of 28° or 42°, on the flow dynamics for the cold-air-pool episode presented in Section 3.2. Comparison of model results is performed both at the local scale (i.e., against meteorological data; Section 4.2) and at the scale of the valley (Section 4.3). A brief presentation of the meteorological data is provided in Section 4.1. All times in Figures 10–15 are UTC.

4.1 | Meteorological data

Meteorological data are available from stations located at three levels in the valley: at the floor, at mid-height, and at the top of the valley. The locations of these stations are indicated in Figure 1 and summarized in Table 2. The air-quality monitoring station referred to in Section 3.2 is also reported in the table.

4.2 | Comparison at the local scale

Time series of hourly observed and simulated zonal and meridional components of the wind at 10 m AGL at Institut Laue-Langevin (ILL) are presented in Figure 10. The simulated wind has a similar temporal variability for the

TABLE 2 Main characteristics of the meteorological stations (ILL, VSD, PlC, CHM) and air-quality station (FRE) in the Grenoble valley referred to in this article.

Station	Site	Latitude, longitude (deg)	Altitude (m AGL)	Variables[a]
ILL	Institut Laue-Langevin	45.206, 5.694	213 (valley floor)	$T_{2,20,60}$, $u_{10,20,60}$, $v_{10,20,60}$
VSD	Le Versoud airfield	45.217, 5.849	219 (valley floor)	T_2, u_{10}, v_{10}
PlC	Peuil de Claix	45.127, 5.647	948 (mid altitude)	T_2
CHM	Chamrousse	45.128, 5.878	1,727 (high altitude)	T_2
FRE	Les Frenes	45.162, 5.735	214 (valley floor)	PM_{10}, $PM_{2.5}$

[a] T stands for the temperature, and u and v are the zonal and meridional wind components respectively; their subscripts refer to the height in meters above ground level (AGL) at which the measurements are available.

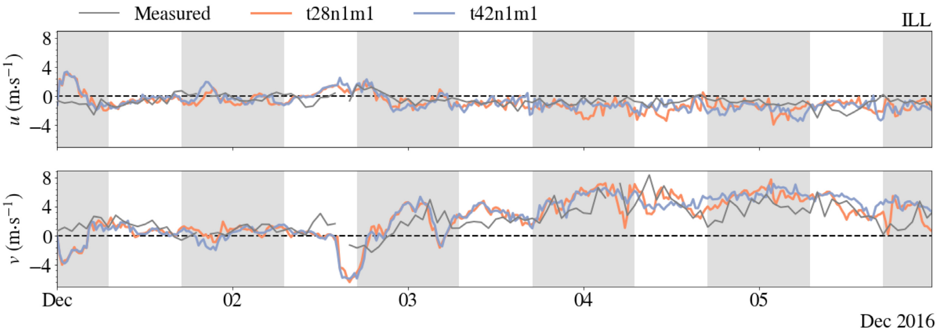

FIGURE 10 Time series of hourly observed and simulated zonal (u) and meridional (v) components of the wind at 10 m above ground level at Institut Laue-Langevin (ILL) for the configurations `t28n1m1` and `t42n1m1` (see Section 2.2 for details of these configurations). The sampling of the time series is 20 min, and a sliding average over 1 hr is performed. The nighttime periods (from sunset to sunrise) are displayed as gray shading.

TABLE 3 Mean absolute error (MAE) and Pearson correlation coefficient (r) for the zonal (u) and meridional (v) components of the wind displayed in Figure 11 for the period December 1–6, 2016, for the configurations `t28n1m1` and `t42n1m1` (see Section 2.2 for details of these configurations).

	MAE (m·s^{-1})		r	
Height (m AGL)	u, v (`t28n1m1`)	u, v (`t42n1m1`)	u, v (`t28n1m1`)	u, v (`t42n1m1`)
10	0.94, 1.85	0.95, 1.97	0.60, 0.78	0.60, 0.80
20	0.93, 1.35	0.93, 1.30	0.54, 0.82	0.56, 0.84
60	1.43, 2.41	1.46, 2.17	0.54, 0.80	0.58, 0.82
100	1.97, 2.60	1.92, 2.33	0.62, 0.76	0.67, 0.79

Abbreviation: AGL, above ground level.

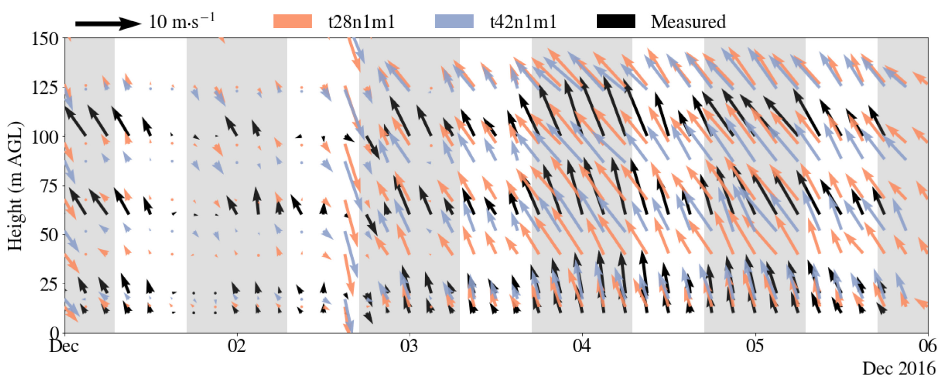

FIGURE 11 Time series of hourly observed and simulated vertical profiles of horizontal wind at Institut Laue-Langevin for the configurations `t28n1m1` and `t42n1m1` (see Section 2.2 for details of these configurations). The sampling of the time series is 20 min, and a sliding average over 3 hr is performed. The nighttime periods (from sunset to sunrise) are displayed as gray shading. AGL: above ground level.

configurations `t28n1m1` and `t42n1m1`. Quantitative statistical metrics are provided in Table 3 and analyzed later herein. Overall, the model simulations reproduce reasonably well the change in wind regime from December 2–3, 2016. Time series for the other two wind measurement sites are not shown here since both observed and simulated winds are very weak at these sites throughout the episode (see Le Bouëdec, 2021).

Wind data are available at several heights on a mast at ILL (10, 20, 60, and 100 m AGL). It is therefore possible to examine the model performance in the lower part of the boundary layer. Figure 11 shows a qualitative comparison of three-hourly observed and simulated vertical profiles of horizontal wind at this site. As for surface winds, the configurations `t28n1m1` and `t42n1m1` give similar results with wind profiles in good agreement with the observations. However, the simulated wind direction is slightly off that observed, with a bias to the west, from December 3, 2016, at 1200 UTC to December 4, 2016, at 1200 UTC. The mean absolute error (MAE) and Pearson correlation coefficient (r) are reported in Table 3. To compute these quantities, model data were interpolated at the heights of the measurements (using cubic splines interpolation; linear interpolation gave similar results).

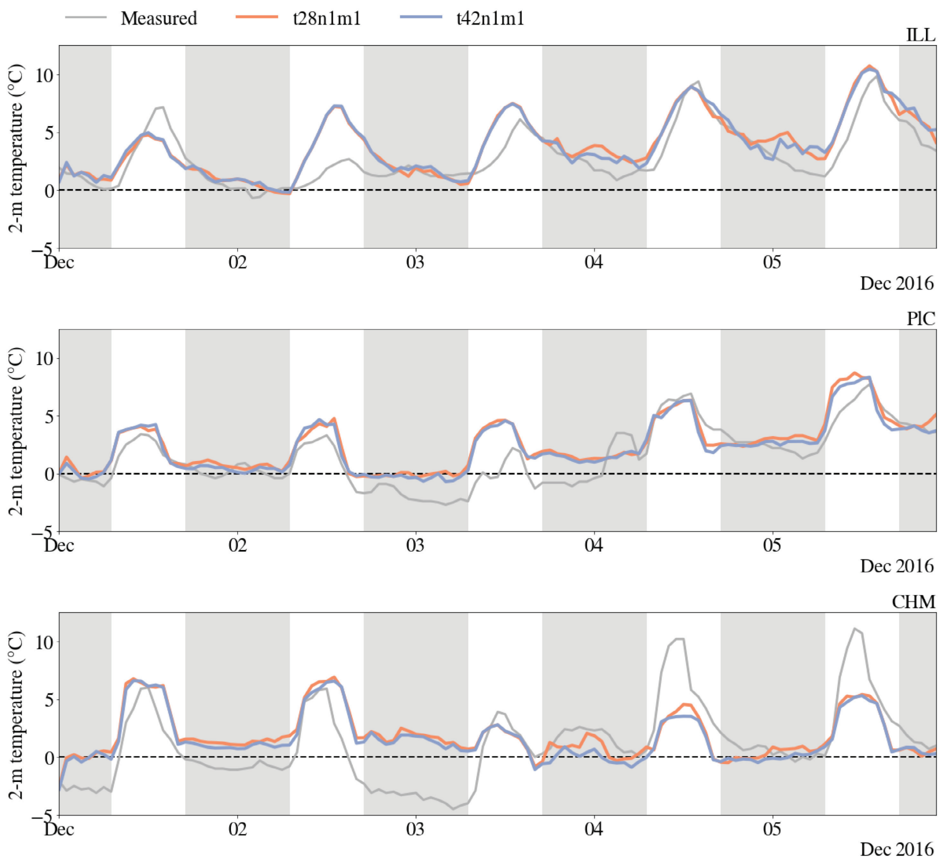

FIGURE 12 Time series of hourly observed and simulated 2-m temperature at Institut Laue-Langevin (ILL), Peuil de Claix (PlC), and Chamrousse (CHM) for the configurations `t28n1m1` and `t42n1m1` (see Section 2.2 for details of these configurations). The sampling of the time series is 20 min, and a sliding average over 1 hr is performed. The nighttime periods (from sunset to sunrise) are displayed as gray shading.

TABLE 4 Mean absolute error (MAE) and Pearson correlation coefficient (r) for hourly 2-m temperature at Institut Laue-Langevin (ILL), Peuil de Claix (PlC), and Chamrousse (CHM) displayed in Figure 12, and at Le Versoud airfield (VSD), for the period December 1–6, 2016, for the configurations `t28n1m1` and `t42n1m1` (see Section 2.2 for details of these configurations)s.

	MAE (K)		***r***	
Site	`t28n1m1`	`t42n1m1`	`t28n1m1`	`t42n1m1`
ILL	1.52	1.55	0.78	0.79
VSD	1.81	1.91	0.83	0.82
PlC	1.62	1.62	0.78	0.78
CHM	2.45	2.46	0.55	0.55

The difference in performance between the configurations `t28n1m1` and `t42n1m1` is not noticeable.

Temperature measurements are staggered on three levels: the valley floor (ILL; Le Versoud airfield, VSD), at mid-height (Peuil de Claix, PlC), and at the top of the valley (Chamrousse, CHM). Time series of hourly observed and simulated 2-m temperature at ILL, PlC, and CHM are presented in Figure 12. The differences between these observed and simulated values are quantified with the MAE and correlation coefficient in Table 4 for the configurations `t28n1m1` and `t42n1m1`. Both configurations capture reasonably well the amplitude of temperature variations at ILL, especially at the end of the episode, although there is a warm bias during the last two nights. The time series for VSD is similar to that for ILL (not shown). The MAE over the episode is between 1.5 K (for ILL) and 1.9 K (for VSD), and the correlation coefficient r is close to 0.8 for the two configurations. This good agreement at the end of the episode is also observed at PlC (MAE = 1.62 K and $r = 0.78$). By contrast, both configurations fail to capture the amplitude of temperature variations at the top of the valley (CHM) and exhibit a cold bias up to 5 K during the last two nights. Consistent with this behavior, the MAE is larger (2.45 K) and the correlation coefficient is smaller (0.55) for both configurations.

Thus, numerical simulations using either configuration `t28n1m1` or configuration `t42n1m1` give very similar results when compared against observations. It is not possible to recommend one configuration over the other

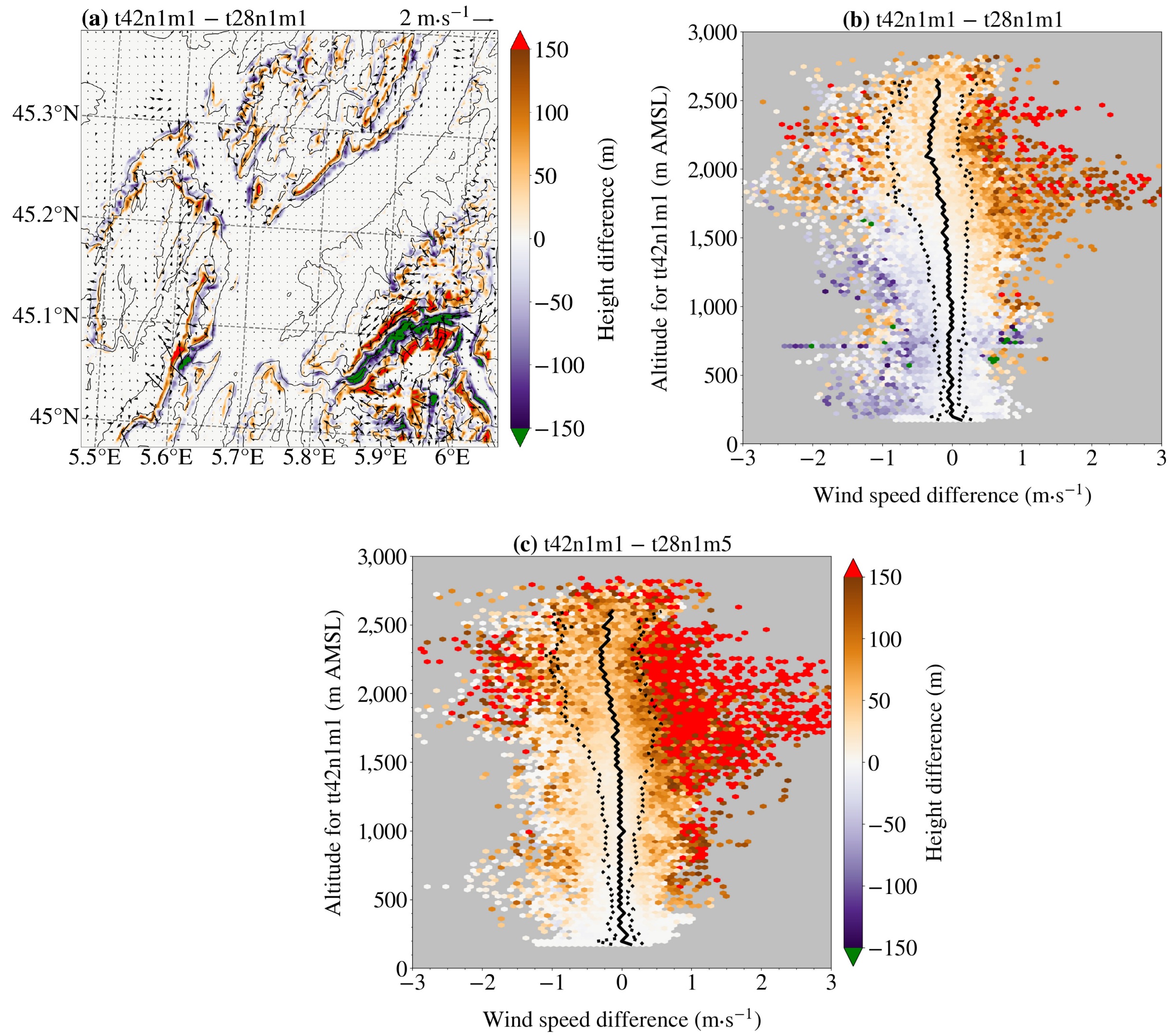

FIGURE 13 (a) Differences in horizontal wind speed at 10 m above ground level between the configurations `t42n1m1` and `t28n1m1` averaged over the period December 1–6, 2016 (see Section 2.2 for details of these configurations). The thin black lines represent isolines of the terrain height, every 500 m, for the configuration `t42n1m1`. (b) Hexagonal bin plot of the wind speed difference between the two configurations at each grid point as a function of altitude for the configuration `t42n1m1`. The hexagons are colored by the terrain height difference between the two configurations. The black continuous line is the median and the dotted lines are the 10th and 90th percentiles. (c) Same as (b) but using the configuration `t28n1m5` in place of the configuration `t28n1m1`. AMSL: above mean sea level.

from this comparison at the local scale. However, this does not imply that the valley-scale dynamics is similar. Differences in the wind and temperature field spatial distributions at that scale are explored in the Section 4.3.

4.3 | Comparison at the valley scale

Model results are now compared at the valley scale through the horizontal wind difference (Section 4.3.1), temperature difference (Section 4.3.2), and vertical temperature gradient and valley heat deficit (Section 4.3.3) in the innermost domain.

4.3.1 | Analysis of the horizontal wind speed difference

Figure 13a displays the differences in episode-averaged horizontal wind speed at 10 m AGL between the configurations `t28n1m1` and `t42n1m1`. A domain-wide view is provided in Figure 13b, which displays this wind speed difference at each grid point of the innermost domain versus the altitude of the point in the configuration `t42n1m1`; each point is colored by the difference in height between the two orographies at its location (each point is actually an hexagon whose color corresponds to the averaged

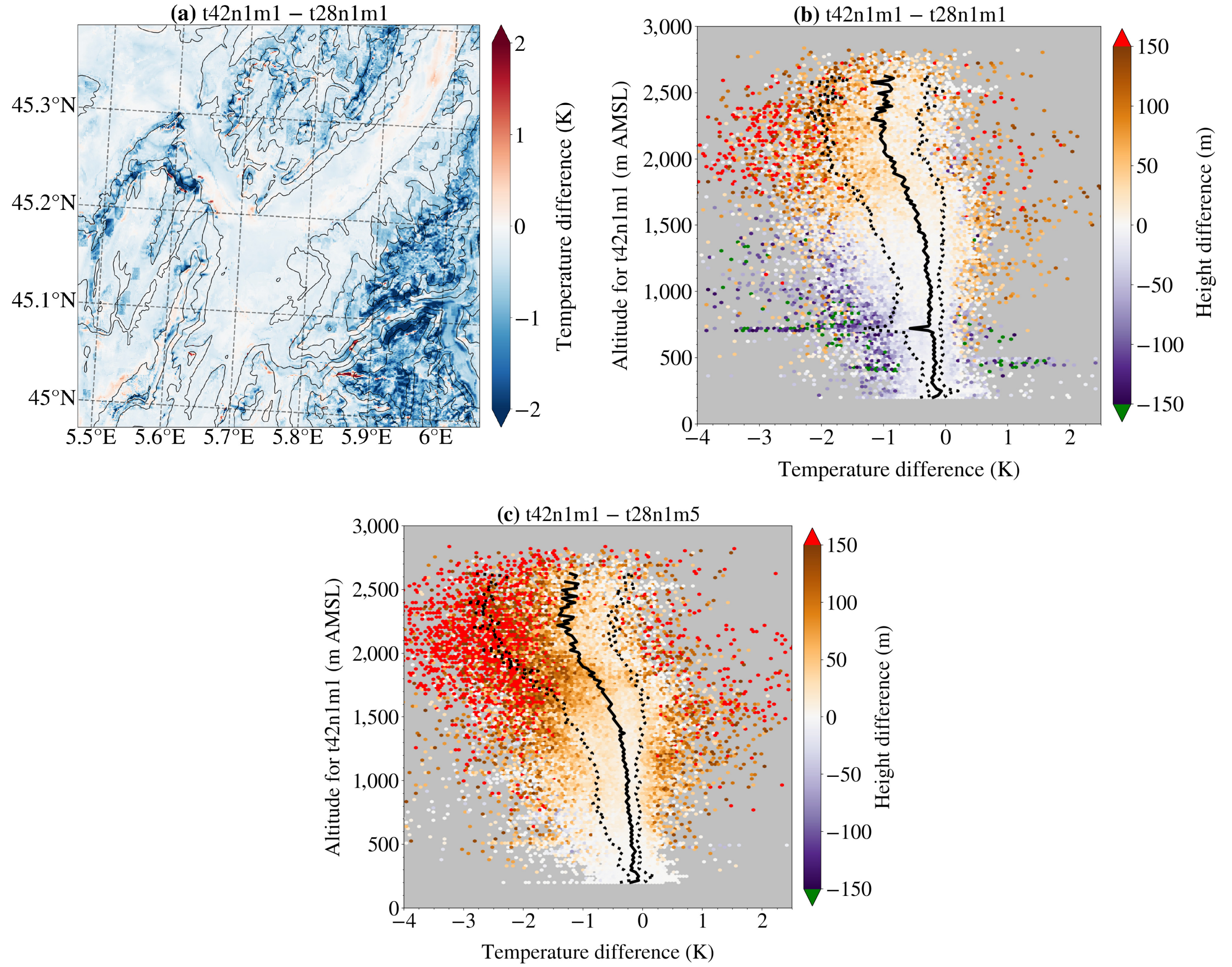

FIGURE 14 (a) Differences in 2-m temperature between the configurations `t42n1m1` and `t28n1m1` averaged over the period December 1–6, 2016 (see Section 2.2 for details of these configurations). The thin black lines represent isolines of the terrain height, every 500 m, for the configuration `t42n1m1`. (b) Hexagonal bin plot of the 2-m temperature difference between the two configurations at each grid point as a function of altitude for the configuration `t42n1m1`. The hexagons are colored by the terrain height difference between the two configurations. The black continuous line is the median and the dotted lines are the 10th and 90th percentiles. (c) Same as (b) but using the configuration `t28n1m5` in place of the configuration `t28n1m1`. AMSL: above mean sea level.

value of the height difference of the points located in the hexagon's surface).

Figure 13a shows that the wind speed differences are very small across the Grenoble valley bottom, much lower than 1 m·s^{-1}. Figure 13b helps quantifying these values: 80% of the wind speed differences at the valley floor are between −0.25 and +0.25 m·s^{-1} (these values are in between the two dashed lines, which represent the 10th and 90th percentiles). Since the along-valley wind speed varies between 2 m·s^{-1} in the Grésivaudan valley to 6 m·s^{-1} in the Voreppe valley (not shown), this implies that the relative wind speed difference at the valley floor is about 10%.

Figure 13b shows that for 80% of the values the wind speed difference is smaller than 0.5 m·s^{-1} in the first 1,500 m above mean sea level (AMSL). This altitude coincides approximately with the top of the inversion layer associated with the cold-air pool that develops in the valley (see Figure 15). Thus, the atmospheric dynamics in the inversion layer is well described by both configurations. The reason is that the difference in height at these grid points is less than about 10 m (as most points are of nearly white color). Above 1,800 m AMSL, 80% of the values are between −1 and +0.5 m·s^{-1}; hence, the range of the wind speed differences broadens.

Figure 13a also shows that the difference in wind speed is large at a few locations where the difference in elevation is greater than 150 m in absolute value. This wind speed difference is about 3 m·s^{-1} along the Vercors cliffs and about 2 m·s^{-1} atop the mountain range around

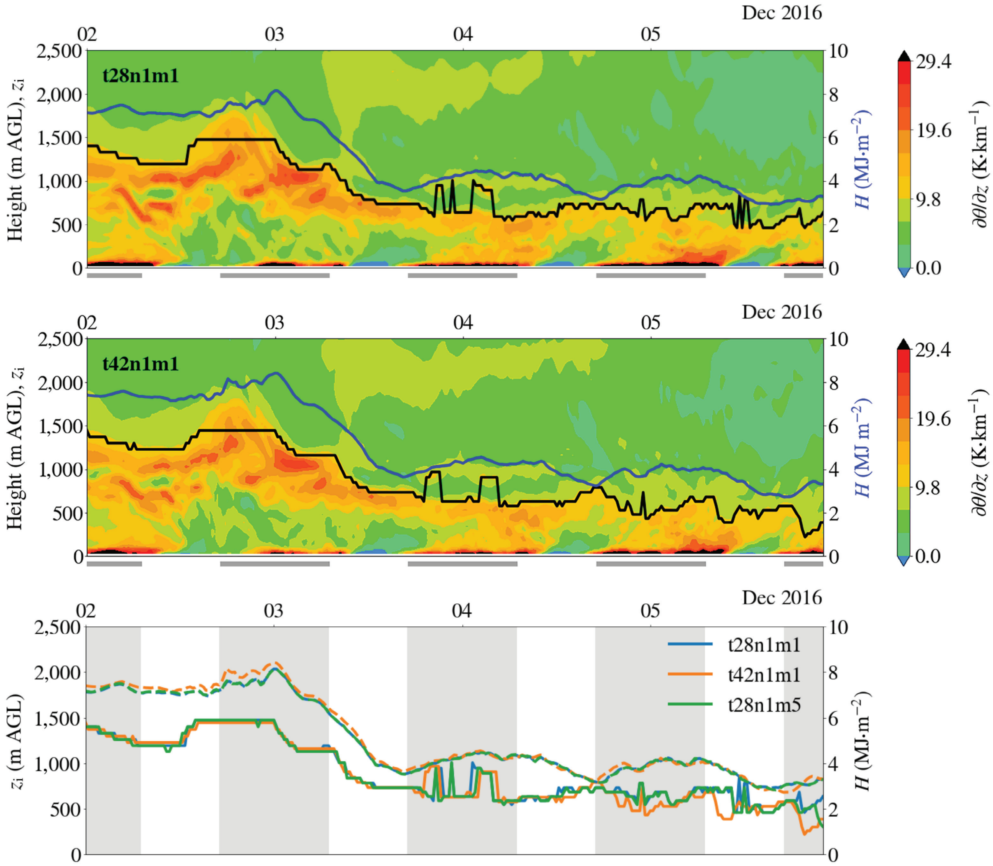

FIGURE 15 Time–height curtain plots of the vertical gradient of potential temperature $\partial\theta/\partial z$, spatially averaged over the Grenoble area (see Figure 1 for the extent of the Grenoble area) for the configurations `t28n1m1` (upper panel) and `t42n1m1` (middle panel). The black line indicates the valley inversion height z_i. The blue line displays the valley heat deficit H below 1,500 m AGL (the values are to be read on the y-axis to the right of the figures). The bottom panel displays the time series of z_i (solid lines, y-axis to the left of the figure) and H (dashed lines, y-axis to the right of the figure) displayed in the two upper panels for the configurations `t28n1m1`, `t42n1m1`, and `t28n1m5` (see Section 2.2 for details of these configurations). The nighttime periods (from sunset to sunrise) are displayed as gray bars below the two top panels and gray shading for the bottom panel.

the Romanche valley. The actual speeds there in `t28n1m1` are about 5 m·s^{-1} and 4 m·s^{-1} respectively (not shown). This implies that the wind speed values differ significantly between the two configurations (by about 50%) at the very few locations where the altitude differs by more than 150 m. Figure 13b helps again making the latter point more quantitative: most extreme wind speed differences (standing above the 90th percentile) are positive, with values up to 3 m·s^{-1} between 1,800 and 2,000 m AMSL. For these points, `t42n1m1` is higher than `t28n1m1` (as indicated by their brown and red colors). Hence, points at a higher altitude in `t42n1m1` have a higher wind speed, a behavior that can be explained by the increase in the large-scale wind speed with altitude.

Figure 13b also shows that median values are very close to zero up to 1,800 m AMSL with a slightly negative value (−0.25 m·s^{-1}) above this altitude.

A peculiar behavior is observed in Figure 13b around 700 m AMSL, which is the altitude of the upper part of the Romanche valley. Significant wind speed differences, as large as 2.5 m·s^{-1}, occur at this location. With the wind speed equal to about 3 m·s^{-1} for the configuration `t28n1m1` (not shown), this leads to a nearly 100% relative difference between the two configurations in the Romanche valley. This peculiar behavior is due to the misrepresentation of the Romanche valley floor for both the configurations `t28n1m1` and `t42n1m1`, because of the absence of penalization factors in the smoothing algorithm ($m = n = 1$; see Section 2.2). This is attested in Figure 13c, which displays the differences in wind speed between the configurations `t42n1m1` and `t28n1m5`: the large values observed around 700 m AMSL are no longer present. (We remind the reader that the smoothing algorithm in configuration `t28n1m5` ensures that the valley bottom stays close to that of the original orography.) This demonstrates the ability of the algorithm to smooth a narrow and steep valley while preserving its valley bottom. However, as also discussed in Section 2.2, this is at the expense of the representation of the summits. All grid points for the configuration `t28n1m5` are indeed (much) lower than their counterparts for the configuration `t42n1m1`, the height difference being larger than 150 m above 1,300 m AMSL (see the red color points in Figure 13c). As a result, wind speed differences exceed 3 m·s^{-1} above that altitude.

Figure 13a has also been produced for the configuration t28n1m5 in Supporting Information Figure S1. Both figures display a very similar wind pattern in the Grenoble valley, implying that the Romanche valley plays no role in the Grenoble valley atmospheric circulation.

4.3.2 | Analysis of the temperature difference

Figure 14a displays the differences in absolute temperature at 2 m AGL between the configurations t28n1m1 and t42n1m1, averaged over the episode. Figure 14b displays the temperature difference at each grid point of the innermost domain versus the altitude of the point in the configuration t42n1m1, with the same meaning for the color scheme as for Figure 13b. Figures similar to Figure 14a,b but involving the configurations t42n1m1 and t28n1m5 are displayed in Supporting Information Figure S2 and Figure 14c respectively. Supporting Information Figure S2 is very similar to Figure 14a, and so it will not be discussed here.

Figure 14a shows that temperature differences are insignificant at the Grenoble valley bottom, which is quantitatively confirmed in Figure 14b: 80% of these values are smaller than about 0.3 K in absolute value. In the inversion layer (below 1,500 m AMSL), the range in these values broadens, but the differences remain smaller than about 1 K in absolute value. Therefore, in that layer, the configurations t42n1m1 and t28n1m1 lead to similar results for the temperature field. By contrast, above the inversion, they differ markedly, with 80% of the values for the temperature differences ranging between −2 K and −0.5 K. A similar conclusion can be drawn when comparing the configurations t42n1m1 and t28n1m5: below 1,200 m AMSL, differences in absolute values are less than 1 K; about that altitude, differences as large as 3 K are observed (see Figure 14c).

Most (over 80%) of the temperature differences displayed in Figure 14b,c are negative. This behavior can be explained as follows. Below a given altitude, the volume of air between the slopes in the configuration t42n1m1 is smaller than in the configurations t28n1m1 and t28n1m5 because the slopes are steeper. The surface areas of the corresponding smoothed orographies are found to differ by less than 1% below the inversion layer. In that layer, the cooling of air occurs mostly through radiative cooling of the neighboring slopes with no long-distance transport of some cold air mass. These arguments imply that, in the inversion layer, the volume of air in the configuration t42n1m1 must be colder than in the configurations t28n1m1 and t28n1m5, which Figure 14b,c attests. Above the inversion layer, assuming the air temperature is that of the free troposphere, the lower orography in the configurations t28n1m1 and especially t28n1m5 with respect to the configuration t42n1m1 (brown and red colors in Figure 14b,c) contributes an additional cooling effect. This argument is consistent with the largest height difference above 1,500 m AMSL in Figure 14c being associated with the largest negative temperature difference.

The misrepresentation of the Romanche valley discussed in Section 4.3.1 has again a marked signature at about 700 m AMSL in Figure 14b. This feature is no longer present in the configuration t28n1m5 (see Figure 14c) for reasons discussed in Section 4.3.1.

4.3.3 | Analysis of the inversion layer

In this section the comparison between the numerical simulations using the configurations t42n1m1 and t28n1m1 is performed by investigating the atmospheric stability in the valley; the simulation using the configuration t28n1m5 is discussed at the end of the section. For this purpose, the vertical gradient of potential temperature ($\partial\theta/\partial z$) averaged over the Grenoble area (defined in Figure 1) is displayed in Figure 15 over the period December 2–5, 2016 (when the large-scale wind is smaller than 10 m·s^{-1}; see Figure 7), for the two configurations. The height of the inversion layer and the heat deficit below 1,500 m computed from these profiles, z_i and H respectively, are also displayed. The valley inversion height is determined as the highest value in altitude below 1,500 m AGL where $\partial\theta/\partial z$ is greater than the dry adiabatic temperature lapse rate (equal to 9.8 K·km^{-1}). The heat deficit is the amount of energy required to fully mix a fluid column of unit area extending from the ground to a given height, taken here as 1,500 m AGL (see Whiteman *et al.*, 1999).

Figure 15 shows that, close to the ground, a strongly stable layer develops during the night, with buoyancy frequency close to 1 rad·s^{-1}, followed during the day by a weakly convective layer at most 50 m deep (consistent with the findings of Largeron & Staquet, 2016). The top of the inversion layer z_i is about 1,500 m AGL during the first 24 hr and drops in about 12 hr to an altitude around 1,000 m AGL. Figure 7 shows that the center of the anticyclone moves away from the Grenoble region from this day on, with the wind direction changing from north to south and strengthening. The stability close to the ground reinforces within the inversion layer, suggesting some downward action of subsidence motions.

Values of the heat deficit H vary from 8 to 4 MJ·m^{-2} over the episode, which are consistent with those computed by Arduini *et al.* (2020), equal to 8–12 MJ·m^{-2}, during a similar cold-air episode in February 2015. The heat deficit correlates very well with the height of the inversion layer (the Pearson correlation coefficient is equal to 0.94).

When z_i and H are compared for the two configurations (see bottom panel of Figure 15), a remarkable agreement is found: the difference in z_i averaged over the period December 2–5 is equal to 66 m and that in H is equal to 0.17 MJ·m^{-2}, amounting to a relative difference of 6% and 3% respectively.

This very good agreement between the two configurations is fully consistent with the previous analysis: it is found in Section 4.3.2 that, within the inversion layer, 80% of the temperature differences between the two configurations are lower (in absolute value) than 0.75 K. It is also found in Section 4.3.1 that 80% of the wind speed differences are smaller than 0.5 m·s^{-1}. Hence, quite remarkably, either configuration can be used to describe the valley atmospheric dynamics in the inversion layer.

The metrics z_i and H computed for the configuration `t28n1m5` are also displayed in the bottom panel of Figure 15. The time series coincide with those for the configuration `t28n1m1` (except for a few spikes due to the computation method). This shows that, at the valley scale and in the inversion layer, a smoothed orography where the valley bottom is everywhere preserved (at the expense of the peaks) can also be used to describe the valley atmospheric dynamics.

5 | CONCLUSIONS

The objective of this article is to evaluate the impact of smoothing orography on the boundary-layer flow in an Alpine valley during a cold-air-pool episode. For this purpose, a global smoothing method, formulated as an optimization algorithm, is designed so as to preserve properties of the orography, such as the mean terrain height. This method is applied to the orography of the Grenoble valley in the French Alps for two maximum slope angles, equal to 28° and 42°, for which 20% and 3% of the innermost domain grid respectively is smoothed by the algorithm. Numerical simulations are then carried out with the WRF model for both slope thresholds to compare the valley flow dynamics in the innermost domain, with horizontal grid spacings equal to 111 m.

Remarkably, not only is the bottom valley dynamics similar for the simulations with slope thresholds of 28° or 42° (and in very good agreement with observations) but this similarity also holds in the whole inversion layer throughout the episode. The results show indeed that, within the inversion layer, 80% of the temperature differences between the two simulations are lower in absolute value than about 1 K, and 80% of wind speed differences are smaller than 0.5 m·s^{-1}. When averaged over the duration of the cold-air-pool episode, the inversion height differs by 3% between the two simulations and the valley heat deficit differs by 6%. The inversion height is generally that of the valley top, about 1500 m above the valley floor for the Grenoble valley. Above the inversion layer, the relative difference in horizontal wind speed reaches 100% at a few locations where the difference in elevation between the smoothed orographies is greater than 150 m (such as the top of the mountain range). The temperature difference at these locations ranges from to 2 to 4 K.

The very good agreement between the two simulations with slope thresholds of 28° or 42° can be explained by the facts that (a) the atmospheric dynamics in the Grenoble valley during the cold-air-pool episode mainly occurs within the inversion layer and (b) the smoothing algorithm barely modifies the valley shape below the inversion layer height (for 80% of the grid points, the largest difference with the original orography for the slope threshold of 28° is about 10 m).

The global smoothing algorithm that we propose includes penalization factors that can be tuned to preserve desired features of the model orography, such as the mean height of the valley floor or of the terrain. The smoothed orography without penalization—with the factors n and m set to 1; see Equation (4)—proved to be appropriate to represent the main valleys of width in the range 3–5 km, whether the slope threshold is equal to 28° or 42°. The numerical simulations with smoothed orography referred to above were performed in this case. However, this was at the expense of a narrow tributary valley of width 1 km and depth 2,000 m, and therefore with steep slopes. The latter valley was indeed poorly represented by the smoothing algorithm with no penalization for either slope angle. Penalization was introduced to handle the smoothing of this steep-slope valley such that the valley bottom stays close to the original orography (at the expense of the peaks). A numerical simulation with the resulting smoothed orography with maximum slope angle equal to 28° led to similar inversion-layer dynamics as those for the non-penalized smoothed orographies. This implies that this tributary valley plays no role in the Grenoble valley inversion-layer dynamics.

Lowering the maximum slope angle from 42° to 28° implies a priori that a finer vertical resolution close to the ground can be used and, therefore, that the boundary flow motions can be better resolved. This is especially important when the atmosphere is stably stratified. We found that the gain in vertical grid size is actually modest: the smallest vertical grid size ensuring numerical stability of the WRF model is equal to 25 m AGL for the slope threshold of 28° and to 32 m AGL for 42° (with the first mass point being located at half this distance from the ground). Further lowering the maximum slope angle below 28° would result in an even larger fraction of the orography modified by the smoothing algorithm, greater than 20%, which could lead to a poorly modeled atmospheric boundary layer in this Alpine valley.

An example of the Python script to solve the optimization problem using the cvxpy package is provided at https://gricad-gitlab.univ-grenoble-alpes.fr/lebouede/wps_dev/-/tree/master/util/topo_smooth.

ACKNOWLEDGEMENTS

Numerical model simulations were performed using high-performance computing resources from GENCI-IDRIS and the ARCHER2 UK National Supercomputing Service.

FUNDING INFORMATION

This work was supported by the French National Research Agency in the framework of the "Investissements d'avenir" program (ANR-15-IDEX-02) through the project CDP IDEX UGA MOBILAIR.

DATA AVAILABILITY STATEMENT

The data that support the findings of this study are available from the corresponding author upon reasonable request.

ORCID

C. Chemel https://orcid.org/0000-0002-6935-7177

REFERENCES

Arduini, G. (2017) Wintertime Stable Boundary-Layer Processes in Alpine Valleys. PhD thesis, Université Grenoble Alpes, Grenoble, France, and University of Hertfordshire, Hatfield, United Kingdom. https://uhra.herts.ac.uk/handle/2299/19706

Arduini, G., Chemel, C. & Staquet, C. (2020) Local and non-local controls on a persistent cold-air pool in the Arve River Valley. *Quarterly Journal of the Royal Meteorological Society*, 146, 2497–2521. Available from: https://doi.org/10.1002/qj.3776

Bohren, C.F. & Beschta, R.L. (1979) Snowpack albedo and snow density. *Cold Regions Science and Technology*, 1, 47–50. Available from: https://doi.org/10.1016/0165-232X(79)90018-1

Büttner, G. (2014) CORINE land cover and land cover change products. In: Manakos, I. & Braun, M. (Eds.) *Land use and Land Cover Mapping in Europe: Practices & Trends. Remote Sensing and Digital Image Processing*, Vol. 18, 5. Dordrecht, Netherlands: Springer, pp. 55–74. Available from: https://doi.org/10.1007/978-94-007-7969-3_5

Chemel, C., Arduini, G., Staquet, C., Largeron, Y., Legain, D., Tzanos, D. et al. (2016) Valley heat deficit as a bulk measure of wintertime particulate air pollution in the Arve River Valley. *Atmospheric Environment*, 128, 208–216. Available from: https://doi.org/10.1016/j.atmosenv.2015.12.058

Chen, F. & Dudhia, J. (2001) Coupling an advanced land surface-hydrology model with the Penn State-NCAR MM5 modeling system. Part I: Model implementation and sensitivity. *Monthly Weather Review*, 129, 569–585. Available from: https://doi.org/10.1175/1520-0493(2001)129<0569:CAALSH>2.0.CO;2

Connolly, A., Chow, F.K. & Hoch, S.W. (2021) Nested large-eddy simulations of the displacement of a cold-air pool by lee vortices. *Boundary-Layer Meteorology*, 178, 91–118. Available from: https://doi.org/10.1007/s10546-020-00561-6

Deardorff, J.W. (1980) Stratocumulus-capped mixed layers derived from a three-dimensional model. *Boundary-Layer Meterorology*, 18, 495–527. Available from: https://doi.org/10.1007/BF00119502

Deppe, A.J., Gallus, W.A. & Takle, E.S. (2013) A WRF ensemble for improved wind speed forecasts at turbine height. *Weather and Forecasting*, 28, 212–228. Available from: https://doi.org/10.1175/WAF-D-11-00112.1

Farr, T.G., Rosen, P.A., Caro, E., Crippen, R., Duren, R., Hensley, S. et al. (2007) The shuttle radar topography mission. *Reviews of Geophysics*, 45, 2005RG000183. Available from: https://doi.org/10.1002/2005RG000183

Hannachi, A., Straus, D.M., Franzke, C.L., Corti, S. & Woollings, T. (2017) Low-frequency nonlinearity and regime behavior in the northern hemisphere extratropical atmosphere. *Reviews of Geophysics*, 55, 199–234. Available from: https://doi.org/10.1002/2015RG000509

Hong, S.-Y., Noh, Y. & Dudhia, J. (2006) A new vertical diffusion package with an explicit treatment of entrainment processes. *Monthly Weather Review*, 134, 2318–2341. Available from: https://doi.org/10.1175/MWR3199.1

Iacono, M.J., Delamere, J.S., Mlawer, E.J., Shephard, M.W., Clough, S.A. & Collins, W.D. (2008) Radiative forcing by long-lived greenhouse gases: calculations with the AER radiative transfer models. *Journal of Geophysical Research*, 113, D13103. Available from: https://doi.org/10.1029/2008JD009944

Jiménez, P.A., Dudhia, J., González-Rouco, J.F., Navarro, J., Montávez, J.P. & García-Bustamante, E. (2012) A revised scheme for the WRF surface layer formulation. *Monthly Weather Review*, 140, 898–918. Available from: https://doi.org/10.1175/MWR-D-11-00056.1

Klemp, J.B., Skamarock, W.C. & Fuhrer, O. (2003) Numerical consistency of metric terms in terrain-following coordinates. *Monthly Weather Review*, 131, 1229–1239. Available from: https://doi.org/10.1175/1520-0493(2003)131<1229:NCOMTI>2.0.CO;2

Largeron, Y. & Staquet, C. (2016) Persistent inversion dynamics and wintertime PM_{10} air pollution in Alpine valleys. *Atmospheric Environment*, 135, 92–108. Available from: https://doi.org/10.1016/j.atmosenv.2016.03.045

Le Bouëdec, E. (2021) *Wintertime Characteristic Atmospheric Circulation in the Grenoble Basin and Impact on Air Pollution*. PhD thesis. Grenoble, France: Université Grenoble Alpes. Available from: https://www.theses.fr/2021GRALU031

Liu, Y., Chen, F., Warner, T. & Basara, J. (2006) Verification of a mesoscale data-assimilation and forecasting system for the Oklahoma City area during the Joint Urban 2003 field project. *Journal of Applied Meteorology and Climatology*, 45, 912–929. Available from: https://doi.org/10.1175/JAM2383.1

Livneh, B., Xia, Y., Mitchell, K.E., Ek, M.B. & Lettenmaier, D.P. (2010) Noah LSM snow model diagnostics and enhancements. *Journal of Hydrometeorology*, 11, 721–738. Available from: https://doi.org/10.1175/2009JHM1174.1

Lu, W. & Zhong, S. (2014) A numerical study of a persistent cold air pool episode in the Salt Lake Valley, Utah. *Journal of Geophysical Research*, 119, 1733–1752. Available from: https://doi.org/10.1002/2013JD020410

Mahrer, Y. (1984) An improved numerical approximation of the horizontal gradients in a terrain-following coordinate system. *Monthly Weather Review*, 112, 918–922. Available from: https://doi.org/10.1175/1520-0493(1984)112<0918:AINAOT>2.0.CO;2

Marjanovic, N., Wharton, S. & Chow, F.K. (2014) Investigation of model parameters for high-resolution wind energy forecasting: Case studies over simple and complex terrain. *Journal of Wind Engineering and Industrial Aerodynamics*, 134, 10–24. Available from: https://doi.org/10.1016/j.jweia.2014.08.007

Meløysund, V., Leira, B., Høiseth, K.V. & Lisø, K.R. (2007) Predicting snow density using meteorological data. *Meteorological Applications*, 14, 413–423. Available from: https://doi.org/10.1002/met.40

Morrison, H., Thompson, G. & Tatarskii, V. (2009) Impact of cloud microphysics on the development of trailing stratiform precipitation in a simulated squall line: Comparison of one- and two-moment schemes. *Monthly Weather Review*, 137, 991–1007. Available from: https://doi.org/10.1175/2008MWR2556.1

Pineda, N., Jorba, O., Jorge, J. & Baldasano, J.M. (2004) Using NOAA AVHRR and SPOT VGT data to estimate surface parameters: Application to a mesoscale meteorological model. *International Journal of Remote Sensing*, 25, 129–143. Available from: https://doi.org/10.1080/0143116031000115201

Quimbayo-Duarte, J., Chemel, C., Staquet, C., Troude, F. & Arduini, G. (2021) Drivers of severe air pollution events in a deep valley during wintertime: A case study from the Arve river valley. *France. Atmospheric Environment*, 247, 118030. Available from: https://doi.org/10.1016/j.atmosenv.2020.118030

Reeves, H.D. & Stensrud, D.J. (2009) Synoptic-scale flow and valley cold pool evolution in the Western United States. *Weather and Forecasting*, 24, 1625–1643. Available from: https://doi.org/10.1175/2009WAF2222234.1

Santos-Alamillos, F., Pozo-Vázquez, D., Ruiz-Arias, J. & Tovar-Pescador, J. (2015) Influence of land-use misrepresentation on the accuracy of WRF wind estimates: Evaluation of GLCC and CORINE land-use maps in southern Spain. *Atmospheric Research*, 157, 17–28. Available from: https://doi.org/10.1016/j.atmosres.2015.01.006

Sheridan, P., Xu, A.L., Li, J. & Furtado, K. (2023) Use of targeted orographic smoothing in very high resolution simulations of a downslope windstorm and rotor in a sub-tropical highland location. *Advances in Atmospheric Science*, 40, 2043–2062. Available from: https://doi.org/10.1007/s00376-023-2298-0

Silcox, G.D., Kelly, K.E., Crosman, E.T., Whiteman, C.D. & Allen, B.L. (2012) Wintertime $PM_{2.5}$ concentrations during persistent, multi-day cold-air pools in a mountain valley. *Atmospheric Environment*, 46, 17–24. Available from: https://doi.org/10.1016/j.atmosenv.2011.10.041

Skamarock, W.C. (2004) Evaluating mesoscale NWP models using kinetic energy spectra. *Monthly Weather Review*, 132, 3019–3032. Available from: https://doi.org/10.1175/MWR2830.1

Skamarock, W.C., Klemp, J.B., Dudhia, J., Gill, D.O., Liu, Z., Berner, J. et al. (2019) A description of the advanced research WRF Version 4. In: *NCAR Technical Note NCAR/TN-556+STR*. Boulder, CO: NCAR. Available from: https://doi.org/10.5065/1dfh-6p97

Smagorinsky, J. (1963) General circulation experiments with the primitive equations. *Monthly Weather Review*, 91, 99–164. Available from: https://doi.org/10.1175/1520-0493(1963)091<0099:GCEWTP>2.3.CO;2

Tomasi, E., Giovannini, L., Zardi, D. & de Franceschi, M. (2017) Optimization of Noah and Noah_MP WRF land surface schemes in snow-melting conditions over complex terrain. *Monthly Weather Review*, 145, 4727–4745. Available from: https://doi.org/10.1175/MWR-D-16-0408.1

Umek, L., Gohm, A., Haid, M., Ward, H.C. & Rotach, M.W. (2021) Large-eddy simulation of foehn–cold pool interactions in the Inn Valley during PIANO IOP 2. *Quarterly Journal of the Royal Meteorological Society*, 147, 944–982. Available from: https://doi.org/10.1002/qj.3954

Vrhovec, T. & Hrabar, A. (1996) Numerical simulations of dissipation of dry temperature inversions in basins. *Geofizika*, 13, 81–96 https://hrcak.srce.hr/18774

Whiteman, C.D., Bian, X. & Zhong, S. (1999) Wintertime evolution of the temperature inversion in the Colorado Plateau Basin. *Journal of Applied Meteorology*, 38, 1103–1117.

Whiteman, C.D., Hoch, S.W., Horel, J.D. & Charland, A. (2014) Relationship between particulate air pollution and meteorological variables in Utah's Salt Lake Valley. *Atmospheric Environment*, 94, 742–753. Available from: https://doi.org/10.1016/j.atmosenv.2014.06.012

Xie, B., Fung, J.C.H., Chan, A. & Lau, A. (2012) Evaluation of non-local and local planetary boundary layer schemes in the WRF model. *Journal of Geophysical Research*, 117, D12103. Available from: https://doi.org/10.1029/2011JD017080

Zängl, G., Gantner, L., Hartjenstein, G. & Noppel, H. (2004) Numerical errors above steep topography: A model intercomparison. *Meteorologische Zeitschrift*, 13, 69–76. Available from: https://doi.org/10.1127/0941-2948/2004/0013-0069

Zhong, S. & Chow, F.K. (2013) Meso- and fine-scale modeling over complex terrain: Parameterizations and applications. In: Chow, F.K., de Wekker, S.F.J. & Snyder, B.J. (Eds.) *Mountain Weather Research and Forecasting: Recent Progress and Current Challenges*, Vol. 10. Dordrecht, Netherlands: Springer Atmospheric Sciences, pp. 591–653. Available from: https://doi.org/10.1007/978-94-007-4098-3_10

SUPPORTING INFORMATION

Additional supporting information can be found online in the Supporting Information section at the end of this article.

How to cite this article: Bouëdec, E.L., Chemel, C. & Staquet, C. (2025) Dealing with steep slopes when modeling stable boundary-layer flow in Alpine terrain. *Quarterly Journal of the Royal Meteorological Society*, 151:e4835. Available from: https://doi.org/10.1002/qj.4835